RESEARCH ARTICLE

National Science Review
7: 1059–1067, 2020
doi: 10.1093/nsr/nwaa039
Advance access publication 9 March 2020

MATERIALS SCIENCE

Paving the road toward the use of β-Fe_2O_3 in solar water splitting: Raman identification, phase transformation and strategies for phase stabilization

Ningsi Zhang[1], Xin Wang[1], Jianyong Feng[1], Huiting Huang[1], Yongsheng Guo[1], Zhaosheng Li[1,2,*] and Zhigang Zou[1,2]

ABSTRACT

Although β-Fe_2O_3 has a high theoretical solar-to-hydrogen efficiency because of its narrow band gap, the study of β-Fe_2O_3 photoanodes for water splitting is elusive as a result of their metastable nature. Raman identification of β-Fe_2O_3 is theoretically and experimentally investigated in this study for the first time, thus clarifying the debate about its Raman spectrum in the literature. Phase transformation of β-Fe_2O_3 to α-Fe_2O_3 was found to potentially take place under laser and electron irradiation as well as annealing. Herein, phase transformation of β-Fe_2O_3 to α-Fe_2O_3 was inhibited by introduction of Zr doping, and β-Fe_2O_3 was found to withstand a higher annealing temperature without any phase transformation. The solar water splitting photocurrent of the Zr-doped β-Fe_2O_3 photoanode was increased by 500% compared to that of the pure β-Fe_2O_3 photoanode. Additionally, Zr-doped β-Fe_2O_3 exhibited very good stability during the process of solar water splitting. These results indicate that by improving its thermal stability, metastable β-Fe_2O_3 film is a promising photoanode for solar water splitting.

Keywords: solar energy conversion, metastable phase, phase transformation, iron oxide, photoelectrochemical water splitting

[1]Collaborative Innovation Center of Advanced Microstructures, National Laboratory of Solid State Microstructures, College of Engineering and Applied Sciences, Nanjing University, Nanjing 210093, China and [2]Jiangsu Key Laboratory of Nano Technology, Nanjing University, Nanjing 210093, China

***Corresponding author.** E-mail: zsli@nju.edu.cn

Received 15 November 2019; **Revised** 11 January 2020; **Accepted** 8 February 2020

INTRODUCTION

Since the concept of a hydrogen economy was introduced, solar hydrogen production using photoelectrochemical (PEC) or photocatalytic water splitting has occupied a very important position in the artificial utilization of inexhaustible solar energy [1–6]. Solar water splitting for hydrogen production has thereby attracted intensive and ever-increasing interest from many researchers [7–15]. The solar-to-hydrogen efficiency of PEC water splitting reached over 19% using III-V multi-junction semiconductors (including In and Ga) prepared by molecular beam epitaxial growth [16]. Unfortunately, there is a lack of low-cost, environmentally friendly, efficient and stable photoelectrodes for PEC water splitting [17–22], thus hindering application of PEC cells for hydrogen production.

In recent decades, iron-based semiconductors with narrow band gaps (e.g. α-Fe_2O_3) have been considered as promising photoanode materials with respect to nontoxicity, cost, stability and theoretical solar-to-hydrogen efficiency [23–34]. Recently, a β-Fe_2O_3 semiconductor with a direct band gap of 1.9 eV was reported by the present authors as a water splitting photoanode under Air Mass 1.5 Global spectrum (AM 1.5 G, 100 mW cm^{-2}) illumination [35]. Theoretically, a β-Fe_2O_3 photoanode for solar water splitting may exhibit a solar-to-hydrogen efficiency of 20.9% because of its narrow band gap of 1.9 eV, whereas its solar photocurrent density is still very low [35]. The phase transformation of metastable β-Fe_2O_3 to mature α-Fe_2O_3 may occur initially at the surface or interface during fabrication of photoanode films because metastable β-Fe_2O_3 cannot withstand the high temperature of annealing.

Phase identification of β-Fe_2O_3 is very important to avoid the effects of impurities (e.g. α-Fe_2O_3) during the process of solar water splitting. Phase characterization of inorganic materials is frequently achieved with such methods as X-ray

diffraction (XRD), neutron diffraction, electron diffraction, Raman scattering spectroscopy and infrared absorption spectroscopy. Among these methods, Raman spectroscopy is fast and highly sensitive toward material surface structural information. However, Raman spectra of β-Fe_2O_3 (including Raman peak position and shape) reported in the literature are often contradictory [36,37]. Thus, this study aims to clarify the debates surrounding the Raman spectra of β-Fe_2O_3.

The wavelength and power of the excitation laser should be chosen carefully during the process of Raman detection. An appropriate wavelength of laser should be selected to enhance the Raman sensibility and minimize the fluorescence emission of the samples. It is equally important that the power of the laser be examined cautiously to avoid the influences of thermal effects caused by the laser, especially for those materials with poor thermal stability. For example, phase transformation of ε-Fe_2O_3 and γ-Fe_2O_3 may take place under laser irradiation [38,39], and β-Fe_2O_3 may be converted into α-Fe_2O_3 upon heat treatment [35,40]. Therefore, low-power laser irradiation is required to avoid phase transformation of the β-Fe_2O_3 samples.

In this study, the influence of laser wavelength and irradiation power on phase transformation of β-Fe_2O_3 to α-Fe_2O_3 was investigated, and the Raman vibrational spectrum of β-Fe_2O_3 was clarified. After being doped with Zr, the particle-assembled β-Fe_2O_3 photoanodes can withstand higher annealing temperatures during the post-treatment process. Therefore, the solar water splitting photocurrent density for the particle-assembled Zr-doped β-Fe_2O_3 photoanodes was improved significantly to 1.2 mA cm^{-2}, which is five times greater than that of pure β-Fe_2O_3 photoanodes. Thus, this study suggests metastable β-Fe_2O_3 films as promising photoanode materials for solar water splitting.

RESULTS AND DISCUSSION

β-Fe_2O_3 belongs to the space group $Ia\bar{3}$, T_h^7. Irreducible representations of the Γ-point phonon modes for β-Fe_2O_3 are shown in Supplementary Table S1. Factor group analysis of β-Fe_2O_3 predicts 49 phonon modes, 22 and 17 of which are Raman active modes and infrared active modes (Supplementary Table S2), respectively. Some Raman vibrational modes of β-Fe_2O_3 were observed in previous studies, whereas Rahman and coworkers reported different Raman spectra for β-Fe_2O_3 [36,37]. To clarify the Raman vibrational modes of β-Fe_2O_3, the Raman scatter spectrum of β-Fe_2O_3 was verified, as shown in Supplementary Fig. S1. Twelve clear vibrational peaks of β-Fe_2O_3 were observed at 158, 169, 234, 258, 274, 314, 328, 368, 386, 397, 522 and 635 cm^{-1} using the 785 nm laser of 0.4 W. These peaks can clearly be distinguished from the Raman vibration peaks of α-Fe_2O_3 (227, 246, 293, 300, 411, 499, and 613 cm^{-1}). Compared to previous results from Liang and van de Krol [36], four new vibrational peaks at 258, 397, 522 and 635 cm^{-1} were observed, whereas the vibrational peak at 208 cm^{-1} was not observed.

The theoretical calculations and experimental values of Raman vibrational peaks are listed in Supplementary Table S3. Among the 22 vibrational modes predicted by the theoretical calculations, only 12 significant peaks were observed in the experiments. Three weak vibrational modes are marked with asterisks. The M10 (383 cm^{-1}) and M11 (389 cm^{-1}) modes merge into one peak (386 cm^{-1}) in the experimental spectrum. As given in Supplementary Fig. S1, typical peaks corresponding to vibrational modes 158 cm^{-1} (T_g), 274 cm^{-1} (T_g), 368 cm^{-1} (T_g) and 386 cm^{-1} (E_g+T_g) can be used as a characteristic spectrum for identifying the phase of β-Fe_2O_3. In addition, the theoretically calculated infrared vibrational peaks and the experimental infrared absorption spectrum are also given in Supplementary Table S4 and Supplementary Fig. S2, respectively.

The metastable β-Fe_2O_3 phase may be converted to the mature α-Fe_2O_3 phase upon laser irradiation of different wavelengths and power. Figure 1 shows the effects of laser wavelength on the Raman spectrum of β-Fe_2O_3. The Raman peaks at 227, 293, 411, 499 and 613 cm^{-1} belonging to α-Fe_2O_3 appeared after irradiation of the β-Fe_2O_3 samples with a 532 nm or 633 nm laser. In the case of 785 nm laser irradiation, the experimental and theoretical Raman peaks for β-Fe_2O_3 match in shape but exhibit a slight shift. These results suggest that a 785 nm laser is ideal for detecting the Raman spectra of metastable β-Fe_2O_3.

Raman spectra mapping images shown in Fig. 2 also indicate phase transformation of the particle-assembled β-Fe_2O_3 films without any necking treatment, in which the α-Fe_2O_3 phase appears when the β-Fe_2O_3 film samples are irradiated with a 10 mW laser of 532 and 633 nm. Scanning electron microscope (SEM) images also suggest this phase transformation. Even when β-Fe_2O_3 was irradiated with a laser of 785 nm with 10 mW power, slight damage of the β-Fe_2O_3 films was observed.

Additionally, the effects of laser power on the Raman spectrum of β-Fe_2O_3 were investigated. When the power of the 785 nm laser is increased, a phase change of β-Fe_2O_3 to α-Fe_2O_3 possibly occurs (Fig. 3). After β-Fe_2O_3 is irradiated by 0.4 mW 785 nm laser for an extended period of 500 s, there

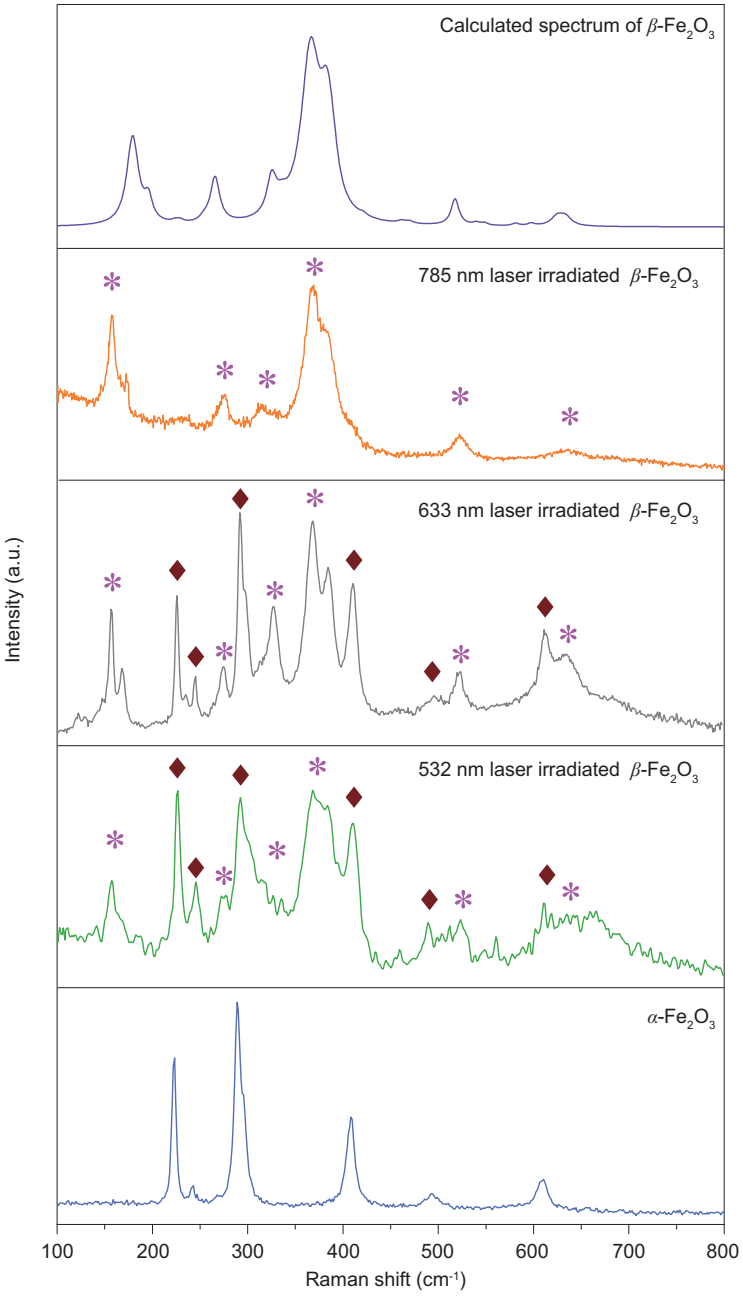

Figure 1. Theoretical calculation and experimental measurement of Raman spectra of β-Fe_2O_3 samples excited by a 0.4 mW laser at 785, 633 and 532 nm. The Raman spectrum of α-Fe_2O_3 is listed as a reference.

is no signal corresponding to α-Fe_2O_3. A significant phase transformation occurs with as little as 2 s irradiation with a 4 mW 785 nm laser. As the laser power increases and the exposure time is prolonged, all the β-Fe_2O_3 gradually converts to α-Fe_2O_3.

Figure 4 shows Raman spectra mapping and SEM images of the particle-assembled β-Fe_2O_3 films without any necking treatment after laser illumination of 785 nm. When the β-Fe_2O_3 films were irradiated with 785 nm laser at 0.4 W power, no α-Fe_2O_3 signal appeared. With the increasing power of the 785 nm laser, the signals of α-Fe_2O_3 were enhanced, suggesting laser-induced phase transformation of β-Fe_2O_3 to α-Fe_2O_3. The SEM images of Fig. 4 also corroborate this result. The phase transformation of β-Fe_2O_3 to α-Fe_2O_3 is initiated by laser irradiation, likely as a result of the thermal effects of the laser. Therefore, low-power laser irradiation is required to avoid the phase transformation of metastable materials during Raman characterization to minimize its thermal effects. Thus, a 0.4 mW 785 nm laser is ideal for measuring the Raman spectra of β-Fe_2O_3.

Figure 5 shows transmission electron microscope (TEM) and selected area electron diffraction (SAED) images of the β-Fe_2O_3 samples. A simulated SAED image of α-Fe_2O_3 is shown in Fig. 5 for comparison. The measured SAED image of β-Fe_2O_3 samples (Fig. 5a) is in good agreement with the simulated SAED image of α-Fe_2O_3 (Fig. 5d) rather than the simulated SAED image of β-Fe_2O_3 samples (Fig. 5c), suggesting that the phase transformation of β-Fe_2O_3 to α-Fe_2O_3 induced by electron irradiation was also observed in this study. Note that the use of SAED to detect β-Fe_2O_3 should be done with caution. The phase transformation of β-Fe_2O_3 to α-Fe_2O_3 may be driven by laser irradiation, electron irradiation and heating (Supplementary Figs S3 and S4).

In our previous work, phase transformation of β-Fe_2O_3 to α-Fe_2O_3 occurred after annealing at 650°C [29]. Phase transformation of β-Fe_2O_3 was also proven by the appearance of the Raman peaks of α-Fe_2O_3 (Supplementary Fig. S3). In this study, Zr was introduced into the metastable β-Fe_2O_3 to inhibit phase transformation of β-Fe_2O_3 to α-Fe_2O_3. The formation energy of $Zr_{0.03}Fe_{1.97}O_3$ (Zr-doped β-Fe_2O_3) was calculated as −0.16 eV relative to pure β-Fe_2O_3, suggesting that Zr can be doped into the lattice of β-Fe_2O_3 to form a more stable structure. The density of states (DOS) for $Zr_{0.03}Fe_{1.97}O_3$ indicates that the band gap of β-Fe_2O_3 does not change obviously by doping Zr (Supplementary Fig. S5).

The XRD pattern of Zr-doped β-Fe_2O_3 (Supplementary Fig. S6) is in good agreement with β-Fe_2O_3 (JCPDS#39–0238), suggesting that there is no impurity phase after doping with Zr. The X-ray photoelectron spectroscopy in Supplementary Fig. S7 shows that Zr was doped into the sample. The absorption spectra of pure β-Fe_2O_3 and Zr-doped β-Fe_2O_3 are shown in Supplementary Fig. S8. After annealing, the band gap of pure β-Fe_2O_3 changed, whereas the band gap of Zr-doped β-Fe_2O_3 did not. In previous work, we have reported that the absorption spectrum of β-Fe_2O_3 varies after different calcining processes [35]. The change in band gap indicates that a phase transformation may

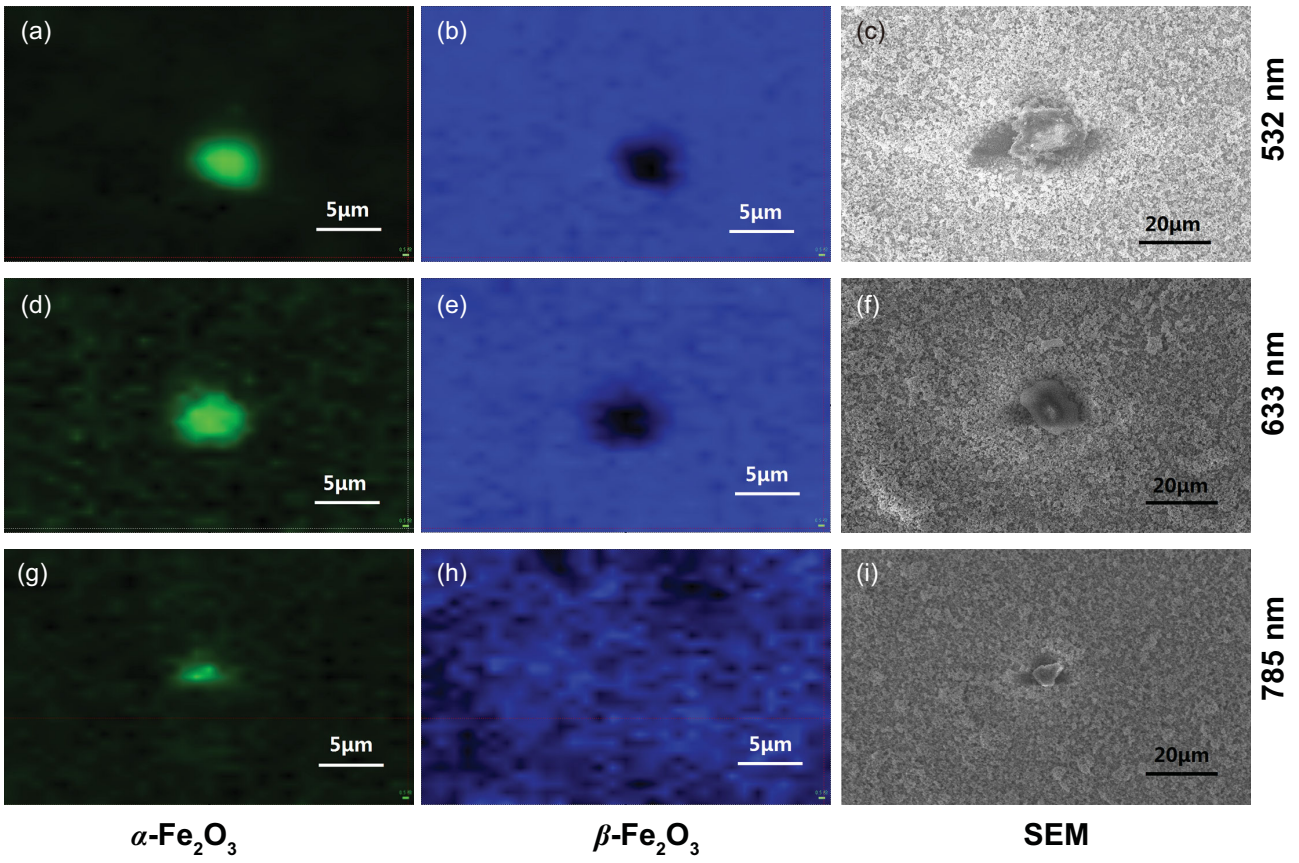

Figure 2. Raman mapping and SEM images of particle-assembled β-Fe_2O_3 films excited by a 0.4 mW laser at 785 nm after irradiation by a 10 mW laser with various wavelengths: (a-c) 532 nm, (d-f) 633 nm and (g-i) 785 nm. (a, d, g) α-Fe_2O_3; (b, e, h) β-Fe_2O_3.

occur. Indeed, after being annealed at 1023 K, the characteristic Raman peaks of α-Fe_2O_3 appeared in the Raman spectrum of the β-Fe_2O_3 sample (Supplementary Fig. S9a), indicating that there was a phase transformation. The Raman spectra of Zr-doped β-Fe_2O_3 did not change after being annealed at 1023 K (Supplementary Fig. S9b), indicating that there was no phase transformation. Note that the results of differential scanning calorimetry show that the phase transition temperature of Zr-doped β-Fe_2O_3 is clearly increased, as shown in Supplementary Fig. S10. The above results show that Zr doping effectively increases the phase transition temperature of metastable iron oxide.

SEM images of the particle-assembled β-Fe_2O_3 photoanodes with and without Zr doping are shown in Supplementary Fig. S11. Figure 6a shows a comparison of the PEC performances of the particle-assembled β-Fe_2O_3 photoanodes with and without Zr doping under AM 1.5 G irradiation (100 mW cm^{-2}). The results show that the photocurrent of Zr-doped β-Fe_2O_3 photoanodes is much higher than that of pure β-Fe_2O_3 photoanodes. Zr-doped β-Fe_2O_3 photoanodes also exhibit much larger monochromatic incident photon-to-electron conversion efficiency (IPCE) than pure β-Fe_2O_3 photoanodes (Fig. 6b). Compared to the pure β-Fe_2O_3, the carrier density of Zr-doped β-Fe_2O_3 has been improved from 1.8×10^{20} to 4.6×10^{20} cm^{-3}, which can be estimated from the Supplementary Fig. S12a. As shown in Supplementary Fig. S12b, the charge separation efficiency of Zr-doped β-Fe_2O_3 is improved by approximately four times at 1.6 V versus Reversible Hydrogen Electrode (RHE), compared to that of β-Fe_2O_3. The increase in the carrier concentration may favor the charge transport and contribute to the improvement in water splitting photocurrent of the Zr-doped β-Fe_2O_3 photoanode.

Under AM 1.5 G irradiation (100 mW cm^{-2}), both Zr-doped and pure β-Fe_2O_3 photoanodes exhibit very good photochemical stability for water splitting during the PEC reaction over 10 h, as shown in Fig. 6c. In the case of particle-assembled Zr-doped β-Fe_2O_3 photoanodes, the Faradaic efficiencies for hydrogen production and oxygen production are 85% and 80%, respectively (Fig. 6d). This result suggests that the photocurrent of the particle-assembled β-Fe_2O_3 photoanodes is mainly attributed to water splitting.

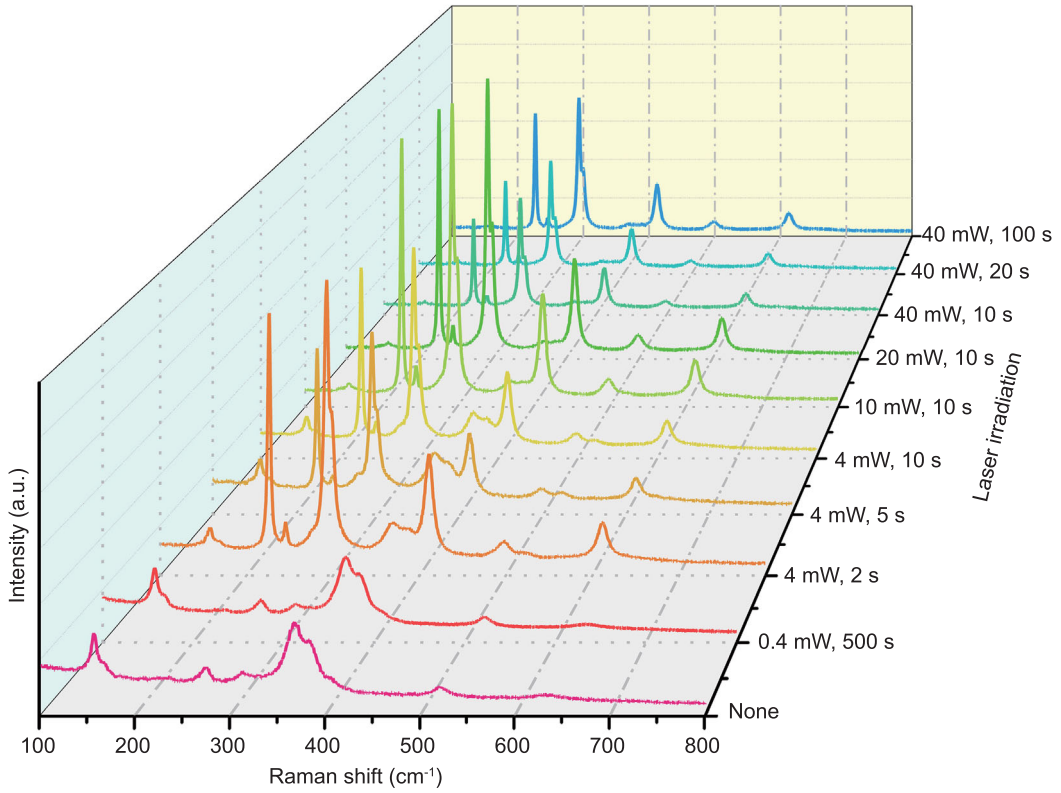

Figure 3. Raman spectra of β-Fe_2O_3 under different power laser irradiations of 785 nm.

During the process of solar water splitting, β-Fe_2O_3 as a photoanode material may be exposed to standard simulated sunlight for a long time. To assess the possibility for phase transformation of β-Fe_2O_3 to α-Fe_2O_3 under simulated sunlight, the Raman spectra of the samples were measured before and after the photochemical stability testing. As shown in Supplementary Fig. S13, the phase of the β-Fe_2O_3 photoanodes before and after the reaction of PEC water splitting remains unchanged. In a typical PEC reaction, the intensity of the light used is not sufficient to promote the phase transformation of β-Fe_2O_3 particle-assembled films. Therefore, β-Fe_2O_3 is a promising photoanode for water splitting. The PEC performance of β-Fe_2O_3 may be improved further by not only the rational design of electrocatalysts but also the optimization of preparation methods [41,42].

CONCLUSION

In conclusion, the Raman spectrum of β-Fe_2O_3 under excitation by a 785 nm laser with 0.4 W power shows 12 significant vibrational modes corresponding to β-Fe_2O_3. The phase transformation of metastable β-Fe_2O_3 to mature α-Fe_2O_3 may be observed under laser irradiation, electron irradiation and heating. Zr doping was introduced to particle-assembled β-Fe_2O_3 films, thus not only increasing the carrier concentration but also suppressing the phase transformation of β-Fe_2O_3. The PEC performance of the Zr-doped β-Fe_2O_3 photoanode was vastly boosted, in comparison with that of the pure β-Fe_2O_3 photoanode. This study demonstrates that metastable β-Fe_2O_3 remains stable during the PEC reaction and is a promising photoanode material for decomposing water, thus paving the road toward the use of β-Fe_2O_3 in solar water splitting (Supplementary Scheme S1).

METHODS

In this study, β-Fe_2O_3 powder was synthesized by calcining the mixture of $NaFe(SO_4)_2$ (or 1.5% $ZrSO_4$ doped $NaFe(SO_4)_2$) and NaCl in a muffle furnace at 450°C for 1 h [43]. As-prepared β-Fe_2O_3 powder was then deposited on fluorine-doped tin oxide (FTO) glass by electrophoretic deposition to prepare the particle-assembled films. In the case of necking treatment for the particle-assembled β-Fe_2O_3 films, 0.2 μmol of $TiCl_4$ in methanol solution was dropped on the particle-assembled β-Fe_2O_3 films. Afterward, the

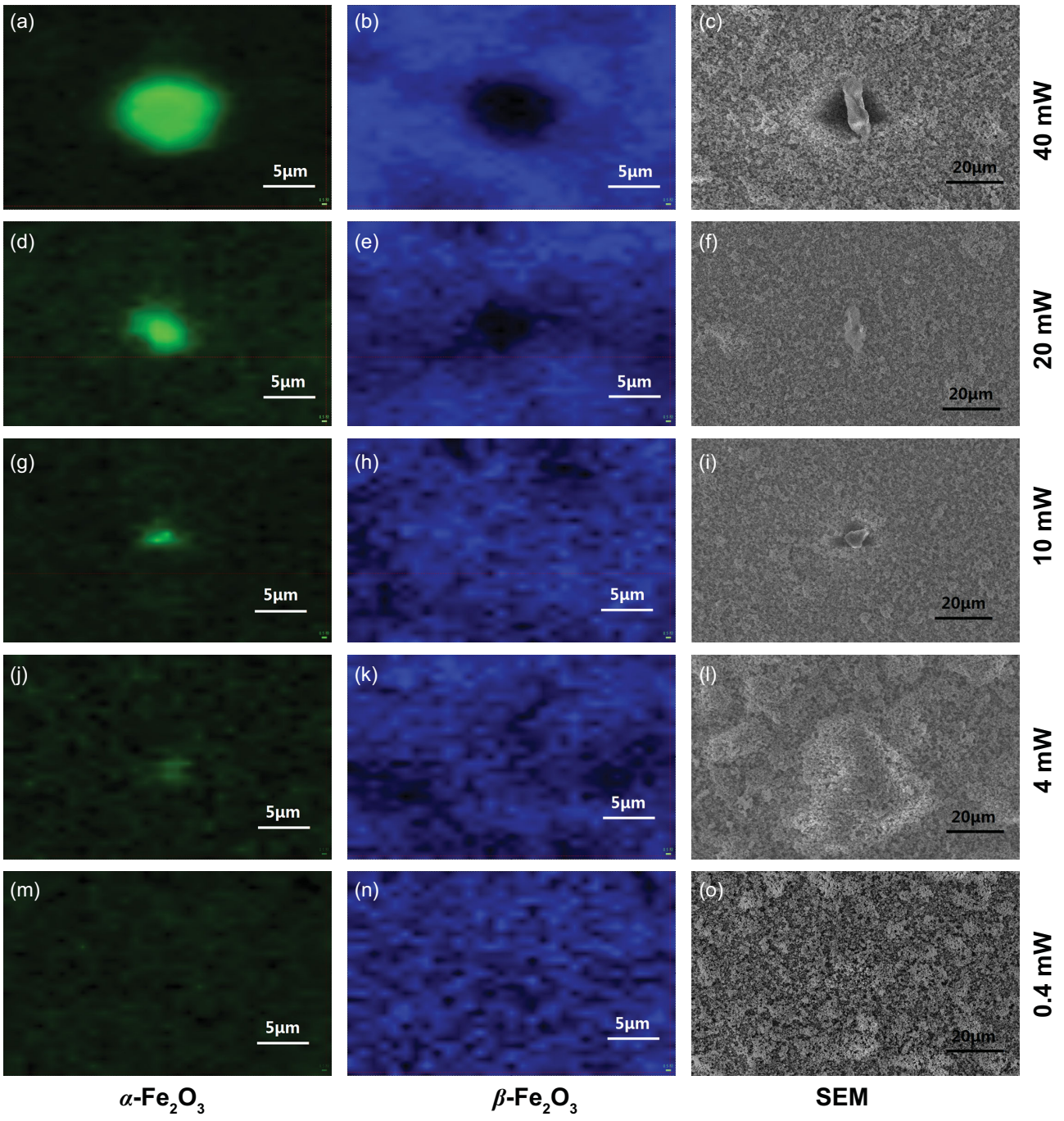

Figure 4. Raman mapping and SEM images of particle-assembled β-Fe_2O_3 films excited by a 0.4 mW laser of 785 nm after the irradiation of 785 nm laser with various power: (a-c) 40 mW, (d-f) 20 mW, (g-i) 10 mW, (j-l) 4 mW and (m-o) 0.4 mW. (a, d, g, j, m) α-Fe_2O_3; (b, e, h, k, n) β-Fe_2O_3.

films were annealed in a muffle furnace at 600°C (or 650°C) for 1 h.

Raman spectra of the samples were characterized with a confocal laser Raman spectrometer (Japan, Horiba, LabRAM Aramis, calibrated with silicon). Except for Fig. 1, all of the Raman spectra data acquisition used a 785 nm laser as the excitation source. Except for Fig. 3, all of the Raman spectra data acquisition used a 0.4 mW power laser as the excitation source. Raman imaging was obtained using a 785 nm, 0.4 mW laser. All laser-induced phase-change samples were confirmed using a 785 nm laser as the excitation source before laser irradiation to ensure that the samples contained no α-Fe_2O_3. The phosphor spectrum calculations were calculated in Material Studio with the Local Density Approximate, using the norm-conserving situation.

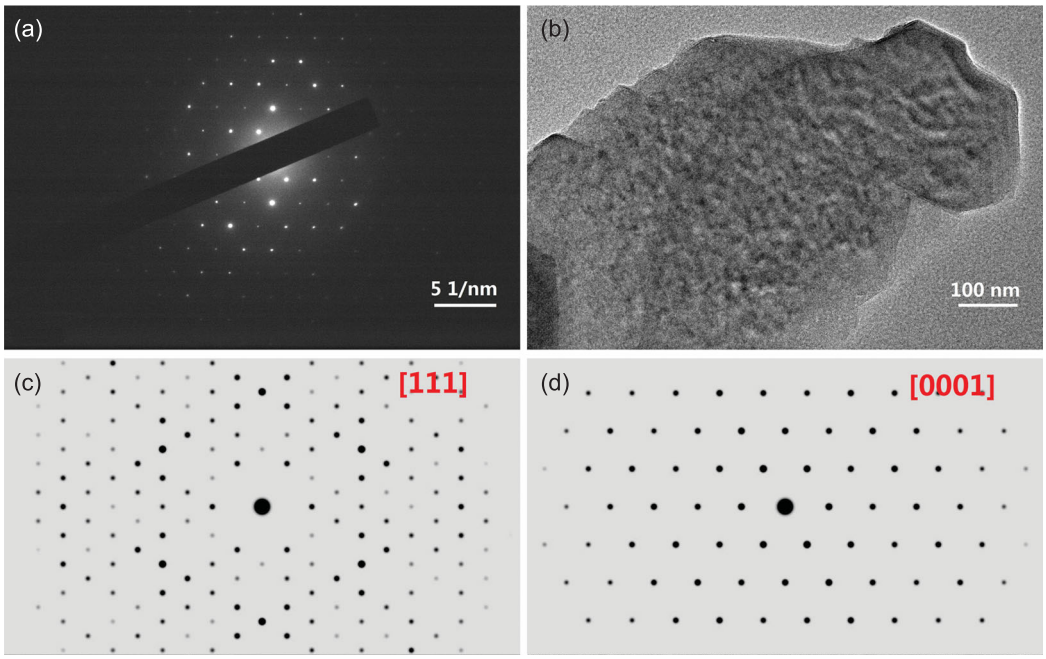

Figure 5. SAED and TEM images of the samples. (a) Measured SAED image of the β-Fe_2O_3 sample. (b) TEM image of the β-Fe_2O_3 sample. (c) Simulated SAED image of β-Fe_2O_3. (d) Simulated SAED image of α-Fe_2O_3.

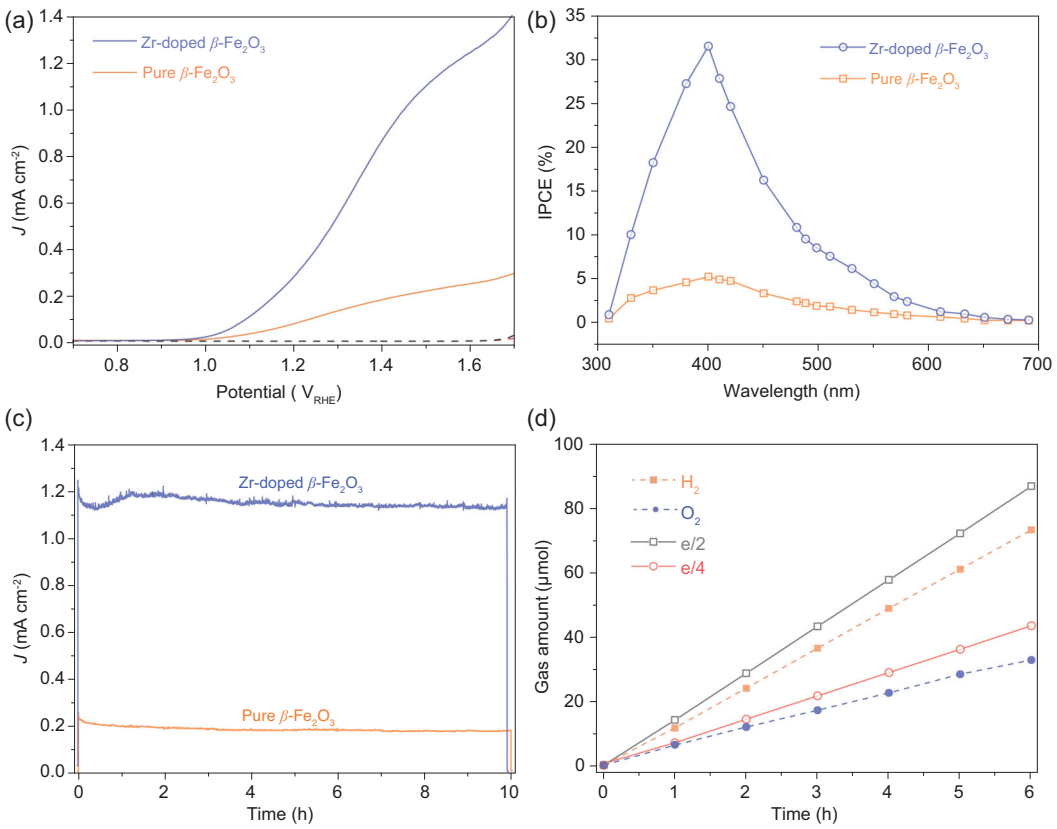

Figure 6. (a) Photocurrent density, (b) IPCE, (c) photochemical stability at 1.6 V_{RHE} and (d) Faradic efficiencies of the particle-assembled β-Fe_2O_3 films with Zr doping under illumination of standard simulated sunlight (100 mW cm^{-2}) in 1 M NaOH electrolyte (pH = 13.6). Reference sample: α-Fe_2O_3.

Density functional theory calculations on Zr-doped β-Fe_2O_3 were implemented in the VASP (Vienna Ab-initio Simulation Package) with a projected-augmented-wave method in the scheme of generalized-gradient approximation, whereas the strong on-site Coulomb repulsion among the localized Fe 3d electrons was described with the generalized-gradient approximation +U approach ('U' is 'the strength of the on-site Coulomb interaction').

SEM images were obtained on an SEM (Germany, Zessis, Ultra 55) and SAED images of the samples were obtained on a TEM (Japan, JEOL, Ltd. JEM2100).

PEC water splitting of the β-Fe_2O_3 particle-assembled films was carried out in 1 M NaOH solution (pH = 13.6) under AM 1.5 G standard simulated sunlight (American, Newport, Oriel Sol3A, 100 mW cm^{-2}).

SUPPLEMENTARY DATA

Supplementary data are available at *NSR* online.

ACKNOWLEDGEMENTS

The characterizations were made at the Collaborative Innovation Center of Advanced Microstructures in Nanjing University. The numerical calculations were conducted thanks to the access to the IBM Blade cluster system at the High Performance Computing Center (HPCC) of Nanjing University.

FUNDING

This work was supported by the National Key Research and Development Program of China (2018YFA0209303), the National Natural Science Foundation of China (U1663228, 51902153 and 51972165) and a project funded by the Priority Academic Program Development of Jiangsu Higher Education Institutions.

Conflict of interest statement. None declared.

REFERENCES

1. Notzel R. InN/InGaN quantum dot electrochemical devices: new solutions for energy and health. *Natl Sci Rev* 2017; **4**: 184–95.
2. Li Z, Luo W and Zhang M *et al.* Photoelectrochemical cells for solar hydrogen production: current state of promising photoelectrodes, methods to improve their properties, and outlook. *Energy Environ Sci* 2013; **6**: 347–70.
3. Han H and Li C. Photocatalysis in solar fuel production. *Natl Sci Rev* 2015; **2**: 145–7.
4. Young JL, Steiner MA and Döscher H *et al.* Direct solar-to-hydrogen conversion via inverted metamorphic multi-junction semiconductor architectures. *Nat Energy* 2017; **2**: 17028.
5. Yang Y, Niu S and Han D *et al.* Progress in developing metal oxide nanomaterials for photoelectrochemical water splitting. *Adv Energy Mater* 2017; **7**: 1700555.
6. Pan L, Kim JH and Mayer MT *et al.* Boosting the performance of Cu_2O photocathodes for unassisted solar water splitting devices. *Nat Catal* 2018; **1**: 412–20.
7. Feng J, Huang H and Fang T *et al.* Defect engineering in semiconductors: manipulating nonstoichiometric defects and understanding their impact in oxynitrides for solar energy conversion. *Adv Funct Mater* 2019; **29**: 1808389.
8. Warren SC, Voïtchovsky K and Dotan H *et al.* Identifying champion nanostructures for solar water-splitting. *Nat Mater* 2013; **12**: 842–9.
9. Li Z, Feng J and Yan S *et al.* Solar fuel production: strategies and new opportunities with nanostructures. *Nano Today* 2015; **10**: 468–86.
10. Pendlebury SR, Wang X and Le Formal F *et al.* Ultrafast charge carrier recombination and trapping in hematite photoanodes under applied bias. *J Am Chem Soc* 2014; **136**: 9854–7.
11. Sivula K and Van De Krol R. Semiconducting materials for photoelectrochemical energy conversion. *Nat Rev Mater* 2016; **1**: 15010.
12. Walter MG, Warren EL and McKone JR *et al.* Solar water splitting cells. *Chem Rev* 2010; **110**: 6446–73.
13. Kment S, Riboni F and Pausova S *et al.* Photoanodes based on TiO_2 and α-Fe_2O_3 for solar water splitting—superior role of 1D nanoarchitectures and of combined heterostructures. *Chem Soc Rev* 2017; **46**: 3716–69.
14. Le Formal F, Pastor E and Tilley SD *et al.* Rate law analysis of water oxidation on a hematite surface. *J Am Chem Soc* 2015; **137**: 6629–37.
15. Zhu Y, Qian Q and Fan G *et al.* Insight into the influence of high temperature annealing on the onset potential of Ti-doped hematite photoanodes for solar water splitting. *Chin Chem Lett* 2018; **29**: 791–4.
16. Cheng W, Richter MH and May MM *et al.* Monolithic photoelectrochemical device for direct water splitting with 19% efficiency. *ACS Energy Lett* 2018; **3**: 1795–800.
17. Klahr B, Gimenez S and Fabregat-Santiago F *et al.* Electrochemical and photoelectrochemical investigation of water oxidation with hematite electrodes. *Energy Environ Sci* 2012; **5**: 7626–36.
18. Klahr B, Gimenez S and Fabregat-Santiago F *et al.* Water oxidation at hematite photoelectrodes: the role of surface states. *J Am Chem Soc* 2012; **134**: 4294–302.
19. Zhao X, Feng J and Wang N *et al.* The influence of Ti doping on morphology and photoelectrochemical properties of hematite grown from aqueous solution for water splitting. *Energy Technol* 2018; **6**: 2188–99.
20. Liang Q, Guo Y and Zhang N *et al.* Improved water-splitting performances of $CuW_{1-x}Mo_xO_4$ photoanodes synthesized by spray pyrolysis. *Sci China Mater* 2018; **61**: 1297–304.
21. Fang T, Huang H and Feng J *et al.* Exploring facile strategies for high-oxidation-state metal nitride synthesis: carbonate-assisted one-step synthesis of Ta_3N_5 films for solar water splitting. *Sci Bull* 2018; **63**: 1404–10.

22. Chen Q, Fan G and Fu H *et al.* Tandem photoelectrochemical cells for solar water splitting. *Adv Phys X* 2018; **3**: 1487267.
23. Wang Z, Mao X and Chen P *et al.* Understanding the roles of oxygen vacancies in hematite-based photoelectrochemical processes. *Angew Chem* 2019; **131**: 1042–6.
24. Xu YF, Wang XD and Chen HY *et al.* Toward high performance photoelectrochemical water oxidation: combined effects of ultrafine cobalt iron oxide nanoparticle. *Adv Funct Mater* 2016; **26**: 4414–21.
25. Qiu Y, Leung SF and Zhang Q *et al.* Efficient photoelectrochemical water splitting with ultrathin films of hematite on three-dimensional nanophotonic structures. *Nano Lett* 2014; **14**: 2123–9.
26. Marelli M, Naldoni A and Minguzzi A *et al.* Hierarchical hematite nanoplatelets for photoelectrochemical water splitting. *ACS Appl Mater Interfaces* 2014; **6**: 11997–2004.
27. Hou Y, Zuo F and Dagg A *et al.* Visible light-driven α-Fe_2O_3 nanorod/graphene/$BiV_{1-x}Mo_xO_4$ core/shell heterojunction array for efficient photoelectrochemical water splitting. *Nano Lett* 2012; **12**: 6464–73.
28. Wang L, Nguyen NT and Huang X *et al.* Hematite photoanodes: synergetic enhancement of light harvesting and charge management by sandwiched with Fe_2TiO_5/Fe_2O_3/Pt structures. *Adv Funct Mater* 2017; **27**: 1703527.
29. Hufnagel AG, Hajiyani H and Zhang S *et al.* Why tin-doping enhances the efficiency of hematite photoanodes for water splitting—the full picture. *Adv Funct Mater* 2018; **28**: 1804472.
30. Malviya KD, Dotan H and Shlenkevich D *et al.* Systematic comparison of different dopants in thin film hematite (α-Fe_2O_3) photoanodes for solar water splitting. *J Mater Chem A* 2016; **4**: 3091–9.
31. Malara F, Fabbri F and Marelli M *et al.* Controlling the surface energetics and kinetics of hematite photoanodes through few atomic layers of NiO_x. *ACS Catal* 2016; **6**: 3619–28.
32. Wang CW, Yang S and Fang WQ *et al.* Engineered hematite mesoporous single crystals drive drastic enhancement in solar water splitting. *Nano Lett* 2015; **16**: 427–33.
33. Sabba D, Kumar MH and Wong LH *et al.* Perovskite–hematite tandem cells for efficient overall solar driven water splitting. *Nano Lett* 2015; **15**: 3833–9.
34. Sun Y, Chemelewski WD and Berglund SP *et al.* Antimony-doped tin oxide nanorods as a transparent conducting electrode for enhancing photoelectrochemical oxidation of water by hematite. *ACS Appl Mater Interfaces* 2014; **6**: 5494–9.
35. Zhang N, Guo Y and Wang X *et al.* A beta-Fe_2O_3 nanoparticle-assembled film for photoelectrochemical water splitting. *Dalton Trans* 2017; **46**: 10673–7.
36. Liang Y and van de Krol R. Influence of Si dopant and SnO_2 interfacial layer on the structure of the spray-deposited Fe_2O_3 films. *Chem Phys Lett* 2009; **479**: 86–90.
37. Rahman MM, Jamal A and Khan SB *et al.* Fabrication of chloroform sensor based on hydrothermally prepared low-dimensional β-Fe_2O_3 nanoparticles. *Superlattices Microstruct* 2011; **50**: 369–76.
38. López-Sánchez J, Serrano A and Del Campo A *et al.* Sol–gel synthesis and micro-Raman characterization of ε-Fe_2O_3 micro-and nanoparticles. *Chem Mater* 2016; **28**: 511–8.
39. El Mendili Y, Bardeau JF and Randrianantoandro N *et al.* Insights into the mechanism related to the phase transition from γ-Fe_2O_3 to α-Fe_2O_3 nanoparticles induced by thermal treatment and laser irradiation. *J Phys Chem C* 2012; **116**: 23785–92.
40. Danno T, Nakatsuka D and Kusano Y *et al.* Crystal structure of β-Fe_2O_3 and topotactic phase transformation to α-Fe_2O_3. *Cryst Growth Des* 2013; **13**: 770–4.
41. Hu Y, Wu Y and Feng J *et al.* Rational design of electrocatalysts for simultaneously promoting bulk charge separation and surface charge transfer in solar water splitting photoelectrodes. *J Mater Chem A* 2018; **6**: 2568–76.
42. Fang T, Huang H and Feng J *et al.* Reactive inorganic vapor deposition of perovskite oxynitride films for solar energy conversion. *Research* 2019; **2019**: 9282674.
43. Danno T, Asoka H and Nakanishi M *et al.* Formation mechanism of nanocrystalline β-Fe_2O_3 particles with bixbyite structure and their magnetic properties. *J Phys Conf Ser* 2010; **200**: 082003.